Journal of Advanced Ceramics
2022, **11**(8): 1208–1221
https://doi.org/10.1007/s40145-022-0604-4
ISSN 2226-4108
CN 10-1154/TQ

Research Article

Self-supported porous heterostructure WC/WO_{3-x} ceramic electrode for hydrogen evolution reaction in acidic and alkaline media

Feihong WANG[a], Binbin DONG[b], Junwei WANG[c], Nianwang KE[a], Chuntian TAN[a], Anding HUANG[a], Yutong WU[a], Luyuan HAO[a], Liangjun YIN[d], Xin XU[a,*], Yuxi XIAN[e,*], Simeon AGATHOPOULOS[f]

[a]*CAS Key Laboratory of Materials for Energy Conversion, Department of Materials Science and Engineering, University of Science and Technology of China, Hefei 230026, China*
[b]*School of Materials Science and Engineering, Henan Key Laboratory of Special Protective Materials, Luoyang Institute of Science and Technology, Luoyang 471023, China*
[c]*Yangtze Delta Region Institute (Huzhou), University of Electronic Science and Technology of China, Huzhou 313001, China*
[d]*School of Energy Science and Engineering, University of Electronic Science and Technology of China, Chengdu 611731, China*
[e]*CAS Key Laboratory of Mechanical Behaviors and Design of Materials, Department of Modern Mechanics, University of Science and Technology of China, Hefei 230026, China*
[f]*Department of Materials Science and Engineering, University of Ioannina, Ioannina GR-451 10, Greece*

Received: January 1, 2022; Revised: April 23, 2022; Accepted: April 25, 2022

Abstract: Tungsten carbide (WC)-based materials are widely considered as the hydrogen evolution reaction (HER) process catalysts due to their "Pt-like" electronic structure. Nonetheless, traditional powder electrodes have a high cost, and display problems related to the process itself and the poor stability over operation time. This paper presented a self-supported asymmetric porous ceramic electrode with WO_{3-x} whiskers formed *in situ* on the walls of the finger-like holes and membrane surface, which was prepared by combining phase inversion tape-casting, pressureless sintering, and thermal treatment in a CO_2 atmosphere. The optimized ceramic electrode displayed good catalytic HER activity and outstanding stability at high current densities. More specifically, it demonstrated the lowest overpotentials of 107 and 123 mV and the lowest Tafel slopes of 59.3 and 72.4 $mV \cdot dec^{-1}$ at 10 $mA \cdot cm^{-2}$ in acidic and alkaline media, respectively. This superior performance was ascribed to the structure of the ceramic membrane and the charge transfer efficiency, which was favored by the *in situ* developed WC/WO_{3-x} heterostructure and the oxygen vacancies.

Keywords: hydrogen evolution reaction (HER); porous ceramic membrane; WC/WO_{3-x} heterostructure; self-supported electrode; oxygen vacancies

* Corresponding authors.
E-mail: X. Xu, xuxin@ustc.edu.cn;
Y. Xian, yxxian@ustc.edu.cn

1 Introduction

Nowadays, energy crisis and environmental pollution have increased the interest in developing sustainable and eco-friendly energy substitutes [1–4]. Hydrogen is a clean, sustainable, and zero-carbon emission energy source, which is widely considered to replace traditional fossil fuels [5–7]. Large scale production of high-purity hydrogen can be obtained by the electrolysis of water [8,9]. Platinum (Pt)-based noble metals are the most effective hydrogen evolution reaction (HER) electrocatalysts, but their high cost and insufficient natural resources severely limit their wide application [10]. Therefore, new electrocatalysts with earth abundance, high efficiency, and high stability must be developed.

Tungsten carbide (WC)-based materials are considered as potential substitutes for Pt in the HER procedure, because they demonstrate a "Pt-like" d-band electron density state owing to the C that inserts into the W lattice [11–14]. WC has abundant resources, and it manifests high chemical stability and excellent electrical conductivity [15]. Traditional WC catalyst synthesis methods, such as W or W-based precursor carbonization process, which is used to prepare nano-WC particles, leading to poor crystallinity and low purity products and limiting the HER activity [11,16]. More importantly, in electrochemical tests or applications, the nano-WC particles need to be casted on the glassy carbon electrode with a polymer binder, which inevitably increases the resistance of charge transfer, buries the active sites, and weakens the catalytic efficiency [17]. Moreover, due to the weak physical contact between the catalyst and the glassy carbon electrode, the coated catalyst is easily peeled off from the electrode during long-term or high-current electrical operation, which severely restricts its stability and durability [18].

Strong attention has been paid on self-supported electrodes, where catalytic active phases could be *in situ* produced on their surfaces. This can improve stability and favor charge transfer and gas transport [17]. In addition, in self-supported electrodes, it is easier to construct the interface by *in situ* reactions and regulate the electronic structure near the interface. Compared with metal- and carbon-based substrates, porous conductive ceramic substrates gained attention recently because of their high chemical stability, tailor-made interconnected porous structure, and high mechanical strength [19,20]. Furthermore, it is worth noting that the inherent hydrophilicity of ceramic surfaces improves electrode/electrolyte contact, which favors charge transfer and bubble detachment [21–23].

Pore structure of electrode plays an important role in its electrocatalytic performance. Phase inversion tape-casting method could be successfully used to fabricate porous ceramic membranes with asymmetric structures [24,25], which could increase the HER performance significantly [19,20]. We combined phase inversion tape-casting and pressureless sintering to prepare the porous WC ceramic membranes with the asymmetric structure. The achieved membranes were suitable for HER; however, the electrocatalytic performance was not satisfactory. The construction of a high catalytic layer in the surface of WC membrane is very important.

Tungsten oxide is an n-type semiconductor material of transition metal oxides. It attracts strong attention in electrocatalysis because of its stability, abundant resources, and environmentally friendly nature [5,26–28]. Nevertheless, the electrocatalytic performance of hexavalent WO_3 suffers from the large bandgap, resulting in poor electronic conductivity [29,30]. Furthermore, the oxide of WO_3 can be partially reduced to produce non-stoichiometric WO_{3-x}. The produced oxygen vacancies provide numerous effective electron transport paths. Therefore, they accelerate electron transport and improve electrical conductivity, as well as can act as active sites to improve the HER performance [2,31–33]. There are currently many methods for preparing WO_{3-x} powders with various morphologies and compositions, such as carbothermal reduction [31], chemical gradient transport reaction [32], thermal evaporation [34], and solvothermal method [35]. Powder composite electrodes based on WO_{3-x} and other active or conductive materials have also been produced, but they exhibit several problems, such as poor stability and compatibility, or complicated preparation processes [5,36,37]. Additionally, a literature survey reveals poor documentation on the *in situ* growth of WO_{3-x} whiskers on WC ceramic membranes for preparing WC/WO_{3-x} composite catalysts for HER.

This paper first prepared a WC ceramic membrane with abundant finger-like holes. Then, the produced WC ceramic membrane was partially oxidized under a CO_2 atmosphere. The aim was to produce WO_{3-x} whiskers with high compatibility to WC, where their *in situ* growth on the membrane surface and inside the

finger-like holes should occur, and be able to be applied to a novel HER self-supported electrode. The HER performance and the self-supported ceramic electrode's long-term and high-current working stability in both acidic and alkaline media were evaluated.

2 Materials and experimental procedures

2. 1 Preparation of WC/WO_{3-x} heterostructure porous ceramic membrane

Commercially available WC (0.5–1 μm; Nangong Jingrui Alloy Material Co., Ltd., China) and tungsten trioxide (WO_3, 1 μm, chemical pure (CP); Sinopharm Chemical Reagent Co., Ltd., China) powders were used for preparing the skeleton of the ceramic membrane. Graphite powders (2 μm, CP; Sinopharm Chemical Reagent Co., Ltd., China) were used to construct the sacrificial layer at the bottom of the membrane. N-methyl-2-pyrrolidone (NMP, CP; Sinopharm Chemical Reagent Co., Ltd., China), polyvinylpyrrolidone (PVP, K30, CP; Sinopharm Chemical Reagent Co., Ltd., China), and polyethersulfone (PESf, Radel A-100; Solvay Advanced Polymers, USA) were used as the solvent, dispersant, and polymer binder of the ceramic slurry, respectively.

The porous WC ceramic membrane was prepared by phase inversion bilayer tape-casting and pressureless sintering, as illustrated in Fig. 1. The compositions of WC and graphite slurries are presented in Table S1 in the Electronic Supplementary Material (ESM). The slurries were obtained by 48-h ball-milling, and then degassed for 40 min. The tape-casting took place afterwards onto a Mylar sheet, using simultaneously two blade-gaps of 0.75 and 0.1 mm for WC and graphite slurries, respectively. The two-layer tape was transferred into a water bath for 6 h, where the phase inversion took place to transform the slurry into a green tape with an asymmetric structure. Then, the product was taken out from the water and dried. The green tape was cut to rectangular samples. The samples were heated at 800 ℃ for 3 h (the heating rate was 5 $K \cdot min^{-1}$) to remove the polymer, and then the temperature was increased to 1600 ℃, followed by holding at 1600 ℃ for 4 h in a graphite furnace under an Ar atmosphere. Then, the obtained WC ceramic membrane was placed in an alumina porcelain boat and heated at various temperatures between 700 and 1000 ℃ for 3 h (the heating rate was 5 $℃ \cdot min^{-1}$) in a tubular furnace under a CO_2 atmosphere to obtain the WC/WO_{3-x} heterostructure ceramic membrane. The obtained samples are hereafter denoted as WC/WO_{3-x}-T (where T = 700, 800, 900, and 1000, representing the heating temperature).

2. 2 Material characterization

The analysis of the crystalline phases developed in the samples was conducted by the X-ray diffractometer (Ultima IV, Rigaku, Japan) using Cu Kα radiation. Their morphologies were observed in a field emission scanning electron microscope (FE-SEM; GeminiSEM 300, ZEISS, Germany) and a transmission electron microscope (TEM; JEM-2100F, JEOL, Japan), equipped with the energy dispersive spectroscopy (EDS) and selected area electron diffraction (SAED) equipments that allowed chemical and crystallographic analysis of the samples.

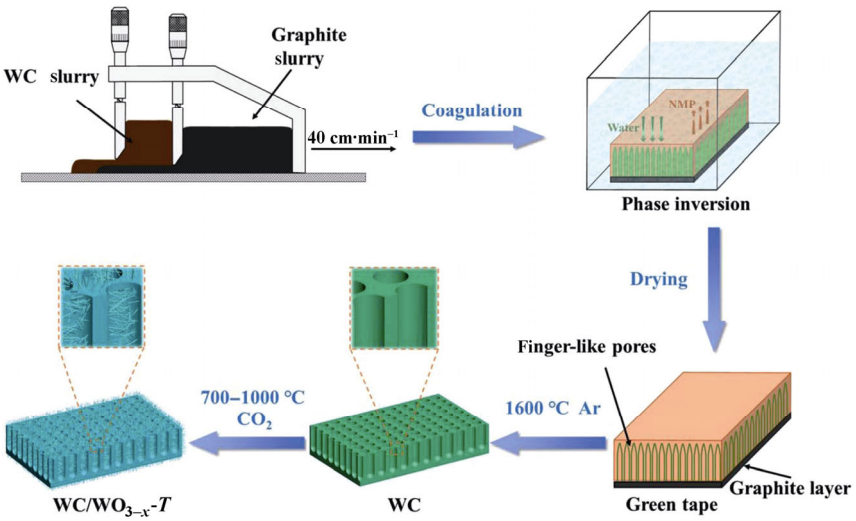

Fig. 1 Preparation process of the porous self-supported WC/WO_{3-x}-T electrodes.

The chemical compositions of the samples were thoroughly analyzed by the X-ray photoelectron spectroscopy (XPS) on a Model Kratos Axis Supra+ equipment (SHIMADZU, Japan) using Al Kα X-ray source. The electron paramagnetic resonance (EPR) spectra were recorded in a JEOL JES-FA200 EPR equipment (JEOL, Japan). The porosity was measured by Archimedes immersion method [25,38]. The mechanical strength of the membranes was estimated by three-point bending strength tests, using an Instron instrument (model 5567, UK, max load cell = 1 kN). Five different rectangular specimens were measured for each sample, and the bending strength (σ_F) was calculated by Eq. (1):

$$\sigma_F = \frac{3FL}{2bh^2} \tag{1}$$

where F is the fracture load, L is the fixture outer span (20 mm), and b and h are the width (10 mm) and thickness (0.6 mm) of the tested sample, respectively. The water contact angle was measured on an Attention Theta equipment (Biolin Scientific, Sweden) at room temperature. The water permeability of the membrane was measured by a self-made device, which was used to evaluate the mechanical and practical properties of the membrane electrode under practical application conditions. The membrane electrode was encapsulated in an interconnecting mold with epoxy, and then attached to a water-filled cylindrical cavity. Various pressures were applied to drive water through the membrane, while measuring the weight of the permeated water with an electronic balance.

2. 3 Electrochemical measurements

The electrochemical test was implemented on the CHI760E electrochemical workstation using a standard three-electrode configuration (Fig. S1 in the ESM), where the prepared porous ceramic membrane was the working electrode, the graphite rod was the counter electrode, and the reference electrodes were Ag/AgCl and Hg/HgO in 0.5 M H_2SO_4 and 1.0 M KOH solutions, respectively. The polarization curves were measured in a saturated N_2 electrolyte at a scan rate of 5 mV·s^{-1} (*IR* compensation was performed). All the potentials of the reversible hydrogen electrode (E_{RHE}) was converted according to Eqs. (2) and (3):

$$E_{RHE} = E_{Ag/AgCl} + 0.0592 \times pH + 0.197 \text{ (0.5 M } H_2SO_4) \tag{2}$$

$$E_{RHE} = E_{Hg/HgO} + 0.0592 \times pH + 0.098 \text{ (1.0 M KOH)} \tag{3}$$

where $E_{Ag/AgCl}$ and $E_{Hg/HgO}$ are the potentials of the Ag/AgCl and Hg/HgO reference electrodes, respectively.

The Tafel slope (b) is the slope of the Tafel equation:

$$\eta = b \log j + a \tag{4}$$

where η is the overpotential, j is the current density, and a is a constant.

The exchange current density (j_0) was calculated by Eq. (4) when the η value is 0. The electrochemical impedance spectroscopy (EIS) was conducted in the range of 100 kHz–0.1 Hz with an amplitude of 5 mV and an overpotential of 200 mV. The double-layer capacitance (C_{dl}) was calculated by the cyclic voltammetry (CV) test at various scan rates (5–30 mV·s^{-1}) to evaluate the electrochemical active surface areas (ECSAs) of the electrocatalysts. The ECSA was calculated according to Eq. (5) [39]:

$$\text{ECSA} = C_{dl}/C_s \tag{5}$$

where C_s is the specific capacitance, and its value is 0.040 mF·cm^{-2}.

The Faradaic efficiency (FE) was calculated by Eq. (6) [40]:

$$\text{FE}(H_2) = \frac{2n_1F_c}{It} \times 100\% \tag{6}$$

where n_1 is the mole of hydrogen, F_c is the Faraday constant (96,485 C·mol^{-1}), and I and t represent the current and time, respectively. The turnover frequency (TOF) was measured and calculated according to Eq. (7) [41]:

$$\text{TOF} = j/(2F_cn_2) \tag{7}$$

where n_2 is the number of active sites. The n_2 values were measured and calculated by the CV test in a potential range of 0–0.6 V vs. RHE and a scan rate of 50 mV·s^{-1}. Then, by integrating the charge over the entire potential range of the CV curve, the half value of the charge was calculated, which represents the surface charge density (Q_s). The value of n_2 was calculated by Eq. (8):

$$n_2 = Q_s/F_c \tag{8}$$

3 Results and discussion

3. 1 Membrane structure

Figure 2(a) presents the X-ray diffraction (XRD) patterns of WC and WC/WO_{3-x}-T. The oxidation products of WC after thermal treatment at 700, 800, 900, and 1000 ℃ were WO_3 (JCPDS No. 20-1324), $W_{19}O_{55}$

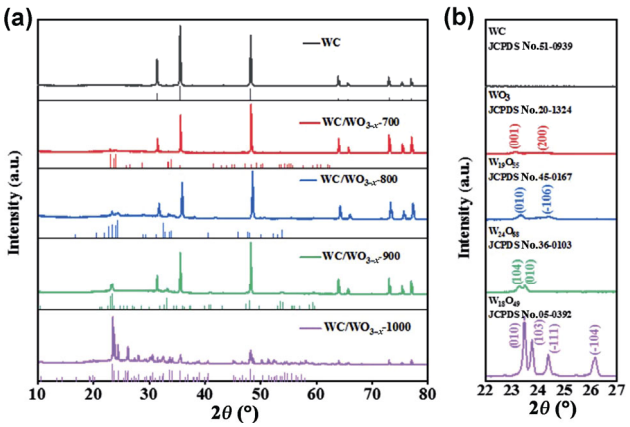

Fig. 2 (a) XRD patterns and (b) enlarged view of the XRD patterns between 22.0° and 27.0°.

(JCPDS No. 45-0167), $W_{24}O_{68}$ (JCPDS No. 36-0103), and $W_{18}O_{49}$ (JCPDS No. 05-0392), respectively. With increasing the thermal treatment temperature, the diffraction peak intensity of WO_{3-x} gradually increased (Fig. 2(b)), while the O/W atomic ratio decreased from 3 to 2.72. Consequently, the thermal treatment temperature directly affected the composition of the produced phase.

Analysis with the XPS sheds light on the chemical states of the produced ceramic electrodes. According to the subsequent HER performance, the sample WC/WO_{3-x}-900 was selected for further detailed analysis. Full XPS spectrum of WC/WO_{3-x}-900 (Fig. S2 in the ESM) revealed the presence of C, N, O, and W elements. Nitrogen should result from the samples' unavoidable exposure to the air. The O 1s spectrum of the WC ceramic membrane (Fig. S3(a) in the ESM) was fitted to two peaks with binding energies of 530.6 and 532.3 eV, corresponding to the W–O and C–O bonds, respectively [42]. This was a result of oxidation that occurred at the sample's surface, along with the presence of a small amount of WO_3 sintering additive [43]. In WC/WO_{3-x}-900 electrode, the O 1s peak (Fig. 3(a)) could be deconvoluted into three peaks. The peak with a binding energy of 530.5 eV represented the W–O bond [31]. The second peak at 531.6 eV should be derived from the oxygen atoms in the region of oxygen vacancies [30,44]. This result further supported that there was a large number of oxygen vacancies on the membrane electrode surface, which could favor the catalytic reaction [44]. The peak at 532.8 eV corresponded to the C–O bond [36]. The O 1s spectra of WC/WO_{3-x}-*T* membranes are presented in Fig. S4 in the ESM. There were no oxygen vacancy peaks in WC

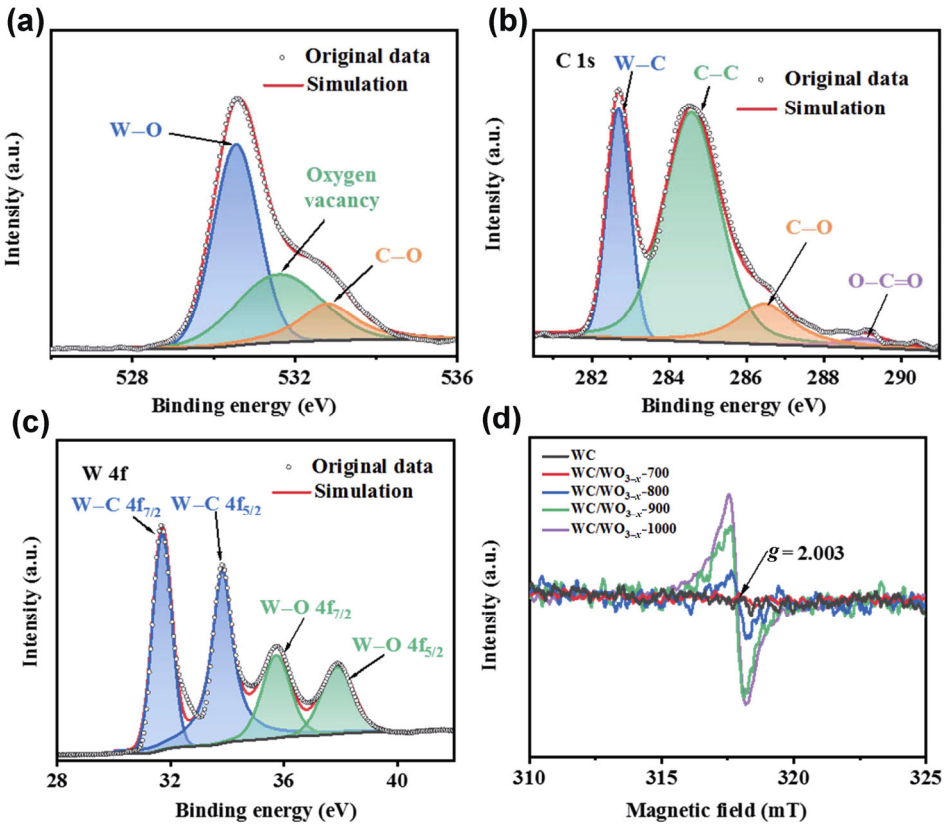

Fig. 3 High-resolution XPS spectra of WC/WO_{3-x}-900 electrode of (a) O 1s, (b) C 1s, and (c) W 4f; and (d) EPR spectra of WC and WC/WO_{3-x}-*T* electrodes.

and WC/WO_{3-x}-700, which was consistent with the XRD and EPR results. However, the oxygen vacancy peak area percentages in WC/WO_{3-x}-800, WC/WO_{3-x}-900, and WC/WO_{3-x}-1000 were 22.6%, 32.5%, and 36.2%, respectively. This suggested that the increase of temperature favored the increase of oxygen vacancy content. The C 1s spectrum of WC/WO_{3-x}-900 electrode (Fig. 3(b)) had three strong peaks originating from the W–C, C–C, and C–O bonds, which were located at 282.7, 284.6, and 286.5 eV, respectively, similar to the WC membrane (Fig. S3(b) in the ESM) [36,45]. The C–O bond was due to the reaction with CO_2, and the C–O bond originally existed in the WC. The other weak peak, located at 288.9 eV, was assigned to the O–C=O bond, also due to the reaction with CO_2 [31].

The W 4f spectrum of WC/WO_{3-x}-900 electrode (Fig. 3(c)) could be deconvolved into 4 characteristic peaks. Among them, a pair of peaks with binding energies centered at 31.7 and 33.8 eV were ascribed to the W–$C_{7/2}$ and W–$C_{5/2}$ bonds, respectively [10,15], while the two distinct peaks at 35.7 and 37.9 eV were attributed to the W–$O_{7/2}$ and W–$O_{5/2}$ bonds, respectively [42,46]. The plots of Fig. S5 in the ESM allow a comparison among the W 4f spectra of WC and WC/WO_{3-x}-*T*. More specifically, the intensity of W–O peaks in WC/WO_{3-x}-*T* gradually increased with the increase of thermal treatment temperature, suggesting that more tungsten oxide was forming by the reaction of WC with CO_2 at high temperatures. Moreover, the binding energy of W 4f in WC/WO_{3-x}-*T* decreased significantly with the increase of temperature. This revealed that WO_3 was reduced partially to produce WO_{3-x} with oxygen vacancies, which was also consistent with the XRD results. Furthermore, in conjunction with the XRD results, the W–O bond in WC/WO_{3-x}-1000 exhibited stronger signals than that in the WC membrane. This provided evidence that WC was over-oxidized by CO_2 at 1000 ℃. The results of the XPS analysis revealed the transfer of electrons at the WC/WO_{3-x} interface (Fig. S6 in the ESM). The binding energy of the characteristic peak of W–C in WC/WO_{3-x}-900 was lower than that of the single-phase WC, and the binding energy of W–O peaks was higher than that of the single-phase WO_3, suggesting that electrons were transferred from WO_{3-x} to WC at the WC/WO_{3-x} hetero-interface. Consequently, this electron transfer effect re-distributed the electrons at the interface and accelerated the charge transfer in electrocatalytic reactions.

Furthermore, the WC and WC/WO_{3-x}-700 membranes had no obvious signal in the EPR spectra (Fig. 3(d)). In contrast, in WC/WO_{3-x}-*T* (*T* = 800, 900, and 1000) electrodes, strong resonance lines appeared at the electron *g* factor of 2.003, which suggested the presence of oxygen vacancies. Moreover, the amount of oxygen vacancies gradually increased with the increase of the thermal-treatment temperature [40,47].

The morphological characteristics of the prepared ceramic electrodes are thoroughly outlined in Fig. 4. More specifically, the cross-section of the WC membrane (Fig. 4(a)) revealed an asymmetric double-layer structure, with a thickness of ~0.6 mm, composed of a skin layer (with a thickness of ~20 μm) and a finger-like porous layer. The finger-like porous layer consisted of many well-arranged micro-channels along the thickness direction. The pores were interconnected by interlacing crystal grains (Fig. S7 in the ESM). The microchannels were open at the bottom surface, had a diameter of ~60 μm, and were named "finger-like holes" after their shape (the inset in Fig. 4(a)). The skin layer at the upper part of the membrane was relatively dense. Its surface morphology, shown in Fig. 4(b), also consisted of interconnected pores formed by crystal grains, with a pore size of ~1 μm.

This unique structure is a result of the phase inversion process. In the water bath, the mutual diffusion of water and NMP destroys the inherent stability of the polymer slurry, resulting in phase separation. Continuous diffusion and phase separation finally lead to form the three-layer membrane structure, consisting of a dense sponge layer at the bottom, a finger-like porous layer in the middle, and a skin layer at the upper part (Fig. S8 in the ESM). Finally, the sponge layer (graphite) is removed after the high-temperature sintering. The skin layer and the finger-like porous layer are retained, forming the asymmetric porous membrane structure with an open bottom surface [48].

When the WC ceramic membrane was thermally treated at 700 ℃ in CO_2, a small number of whiskers with a 200–300 nm diameter grew on the top surface and inside the finger-like holes (Fig. 4(c) and Fig. S9(a) in the ESM). At 800 ℃, the number of whiskers increased, the diameter increased to 200–400 nm, and they were apparently slightly larger (Fig. 4(d) and Fig. S9(b) in the ESM). When the temperature increased to 900 ℃, more whiskers with a diameter of 300–500 nm were produced and uniformly distributed and interlaced

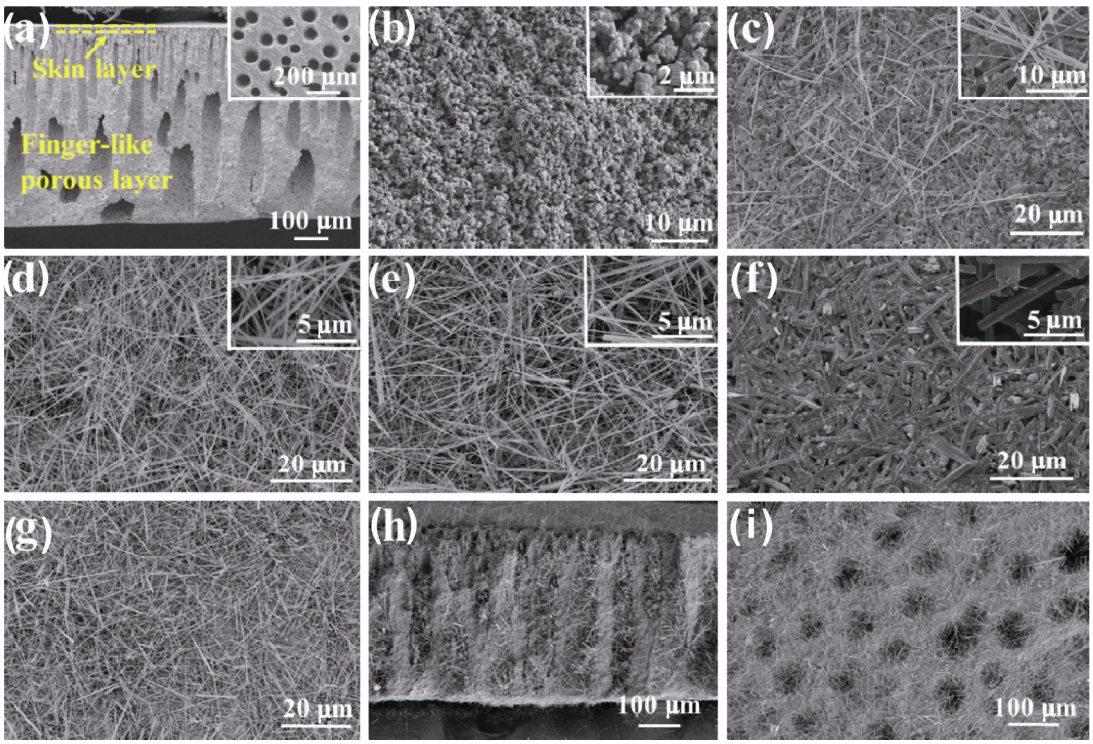

Fig. 4 Microstructures of the ceramic electrodes. (a) Cross-section (the inset shows the bottom surface) and (b) top view of WC; top view of WC/WO_{3-x}-*T* membranes thermal-treated at (c) 700 ℃, (d) 800 ℃, (e) 900 ℃, and (f) 1000 ℃ (the insets show the magnified views); and (g) top view, (h) cross-section showing the finger-like porous layer, and (i) bottom view of WC/WO_{3-x}-900 membrane.

to form interconnected pores, which completely covered the membrane surface and the finger-like hole walls (Figs. 4(e) and 4(g)–4(i)). At 1000 ℃, the diameter of the whiskers was 1.4–2.2 μm, and large pores were formed by interlacing each other (Fig. 4(f) and Fig. S9(c) in the ESM).

At high temperatures, CO_2 should be decomposed into CO and O_2 through Reaction (9) [49]:

$$2CO_2 \rightleftharpoons 2CO + O_2 \quad (9)$$

where at 1000 K: the standard molar reaction Gibbs free energy $\Delta_r G_m^\Theta = 391.25\ \text{kJ}\cdot\text{mol}^{-1}$, the standard equilibrium constant $K^\Theta = 3.65\times10^{-21}$, partial pressure of CO $P_{CO} = 1.9\times10^{-7}$ atm; at 1200 K: $\Delta_r G_m^\Theta = 356.49\ \text{kJ}\cdot\text{mol}^{-1}$, $K^\Theta = 3.03\times10^{-16}$, $P_{CO} = 8.5\times10^{-6}$ atm.

The O_2 with low partial pressure can oxidize WC to WO_3. Through Reaction (10) [50,51]:

$$WC + 4CO_2 \rightleftharpoons 5CO + WO_3 \quad (10)$$

where at 1000 K: $\Delta_r G_m^\Theta = 65.57\ \text{kJ}\cdot\text{mol}^{-1}$, $K^\Theta = 3.76\times10^{-4}$; at 1200 K: $\Delta_r G_m^\Theta = 44.27\ \text{kJ}\cdot\text{mol}^{-1}$, $K^\Theta = 1.18\times10^{-2}$.

Although the standard equilibrium constants at 1000 and 1200 K were lower than 1, Reaction (10) certainly took place spontaneously to the right, because the partial pressure of CO was very low.

The growth of whiskers should take place through the vapor–solid (VS) mechanism [52], because WO_3 sublimated easily. More specifically, CO_2 released trace amounts of oxygen at high temperatures, which should oxidize the WC surface to form the WO_3 crystal nuclei. The formed crystal nuclei grew along the preferred growth direction in the thermodynamic system. A small amount of WO_3 whiskers was produced after thermal treatment at 700 ℃ due to the very low partial pressure of O_2. As the temperature increased, the whiskers' diameter increased due to the higher oxygen partial pressure. The thermal-treatment temperature of 900 ℃ lead to the formation of a large amount of $W_{24}O_{68}$ whiskers with appropriate diameter, which resulted in the best HER performance. Nonetheless, over-oxidation occured at higher thermal treatment temperatures, where $W_{19}O_{48}$ whiskers were too large in diameter, and most of the surface was covered with oxide. When the temperature increased, the high-valence WO_3 should also be easily decomposed to produce low-valence tungsten oxides ($W_{24}O_{68}$, $W_{18}O_{49}$, etc.) [52,53]. The gradual decreased O/W atomic ratio in the

tungsten oxides produced at higher temperatures lead to an increase in oxygen vacancies [52,54].

The mechanical strength and the porosity of the prepared ceramic electrodes are shown in Fig. S10 in the ESM. The bending strength of the pristine WC ceramic membrane was 76.9 MPa, and the strength gradually decreased from 73.6 to 63.2 MPa with the increase of thermal-treatment temperature from 700 to 1000 ℃. It should also be mentioned that all the bending strength values measured were high enough for its wide application. The porosity increased from 58.2% for WC to 67.1% for WC/WO_{3-x}-1000 membrane, attributed to the sublimation of WO_3.

Figure 5 shows the TEM analysis of WC/WO_{3-x}-900 electrode. More specifically, the $W_{24}O_{68}$ whiskers had a diameter of ~400 nm (the inset in Fig. 5(a)). Well-defined lattice fringes of the whiskers displayed good crystallinity with a lattice spacing of 0.379 nm, which corresponded to the (010) plane of $W_{24}O_{68}$ (Fig. 5(a)). The corresponding fast Fourier transform (FFT) image (the inset in Fig. 5(a)) revealed the (010) and the (−500) planes, suggesting the preferential growth of $W_{24}O_{68}$ whiskers along the (010) plane. The interface of WC/$W_{24}O_{68}$ heterostructure was clearly seen in Fig. 5(b). The lattice fringes had a spacing of 0.282 and 0.379 nm, which were assigned to the (001) plane of WC and the (010) plane of $W_{24}O_{68}$, respectively. The decomposition of WO_3 at high temperatures favored the formation of defects, such as lattice distortion, vacancies, and edge dislocation structures (Figs. 5(c), 5(d), and 5(e), respectively), which favored the catalytic activity of the membrane electrodes [55,56].

3. 2 HER electrocatalytic activity

The HER electrocatalytic activity of the prepared ceramic electrodes was evaluated using a typical three-electrode system in 0.5 M H_2SO_4 and 1.0 M KOH media (Fig. S1 in the ESM). The HER catalytic performance of the prepared electrodes, along with the performance of Pt wire electrode in 0.5 M H_2SO_4, is illustrated in Fig. 6 and Table S2 in the ESM. The polarization curves (Fig. 6(a)) after *IR* compensation shows that Pt exhibited the lowest overpotential (defined as the overpotential when the current density reached 10 mA·cm^{-2}) of 34.8 mV. The bare WC ceramic electrode showed the weakest catalytic activity, with an overpotential of 216 mV. The presence of WO_{3-x} significantly improved the catalytic activity, and WC/WO_{3-x}-900 showed the lowest overpotential of 107 mV. The improvement of the catalytic activity could be ascribed to the synergistic effect of tungsten oxide and WC.

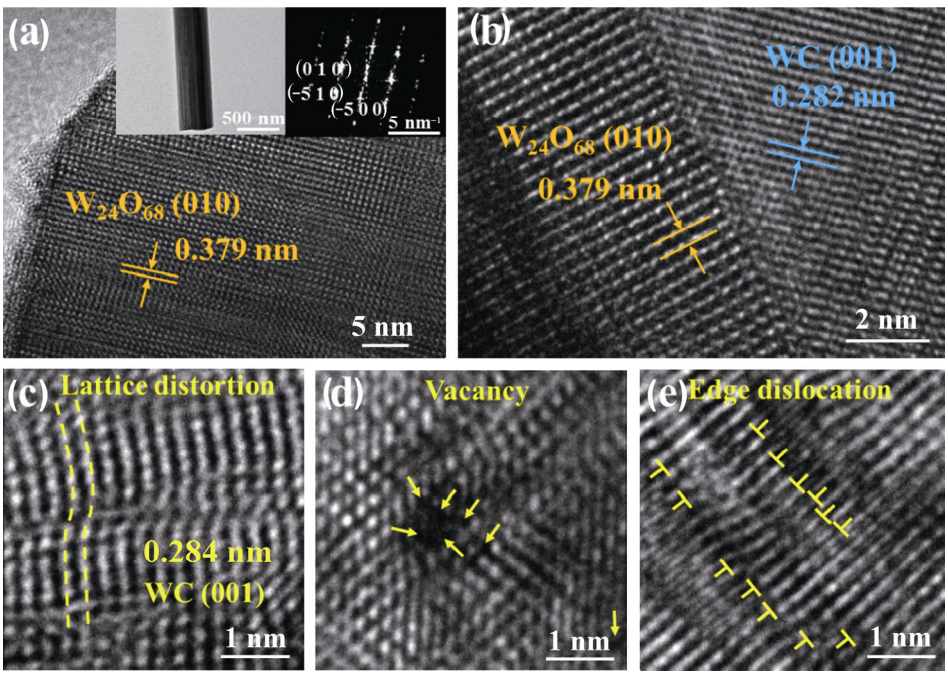

Fig. 5 TEM analysis of WC/WO_{3-x}-900 electrode. (a) HRTEM image of $W_{24}O_{68}$ (the insets are TEM (left) and FFT (right) images), (b) HRTEM image of WC/$W_{24}O_{68}$ heterostructure, and (c–e) TEM images of defects.

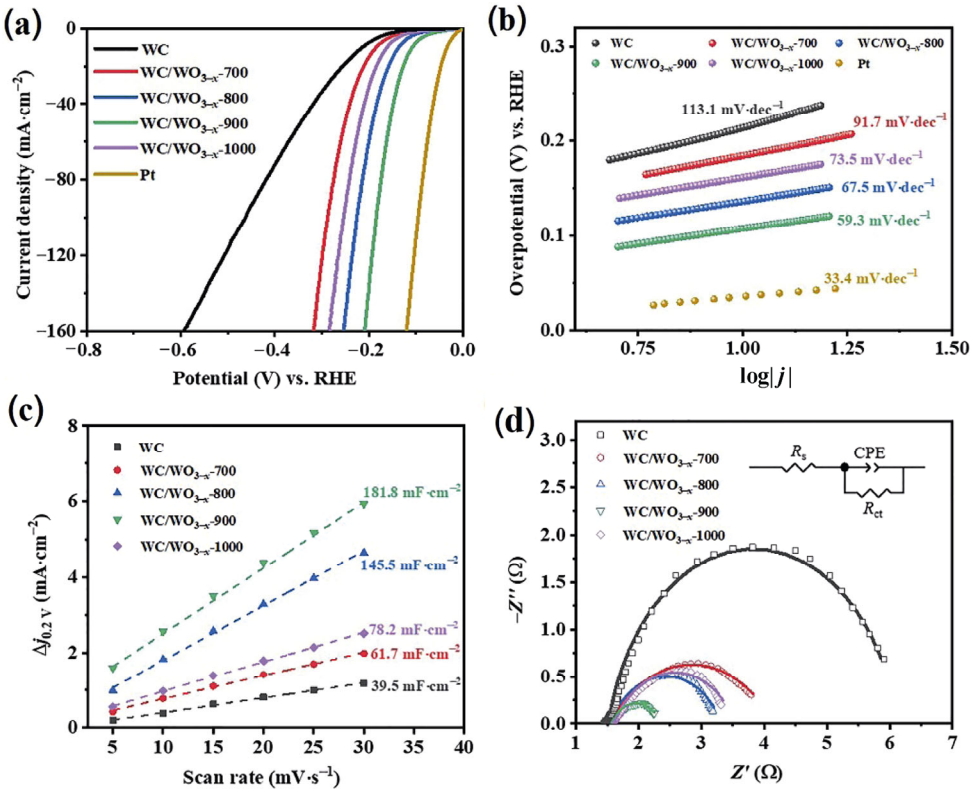

Fig. 6 HER performance of WC and WC/WO_{3-x}-*T* ceramic membrane electrodes thermal-treated at 700, 800, 900, and 1000 ℃ and comparison with commercial Pt wire electrode in 0.5 M H_2SO_4 media. (a) Polarization curves, (b) Tafel slope plots, (c) capacitive current density ($\Delta j_{0.2\ V}$) as a function of scan rate, and (d) EIS plots at an overpotential of 200 mV (the inset presents the equivalent circuit).

The Tafel slope is used to elucidate the kinetics of the electrocatalytic reaction process. The Tafel plots (Fig. 6(b)) demonstrated that the Tafel slope of Pt was 33.4 mV·dec^{-1}, which was close to the value reported in Ref. [57]. The Tafel slope of WC/WO_{3-x}-900 was 59.3 mV·dec^{-1}, which was superior to those of WC (113.1 mV·dec^{-1}), WC/WO_{3-x}-700 (91.7 mV·dec^{-1}), WC/WO_{3-x}-800 (67.5 mV·dec^{-1}), and WC/WO_{3-x}-1000 (73.5 mV·dec^{-1}), manifesting the fastest kinetics.

In an acidic medium, the HER process can be carried out through the following three basic steps [42]:

$$\text{Volmer reaction} \quad H_3O^+ + e^- \rightarrow H_{ads} + H_2O \quad (11)$$

$$\text{Heyrovsky reaction} \quad H_3O^+ + e^- + H_{ads} \rightarrow H_2\uparrow + H_2O \quad (12)$$

$$\text{Tafel reaction} \quad H_{ads} + H_{ads} \rightarrow H_2\uparrow \quad (13)$$

According to the slope values, the Volmer–Heyrovsky mechanism should govern the HER process in WC/WO_{3-x}-900 electrode.

The exchange current density (j_0) is also an important parameter for evaluating the HER kinetics. It represents the hydrogen evolution rate per unit surface area at a certain potential, and can be calculated by extrapolating the Tafel diagram [58]. The results (Fig. S11 and Table S2 in the ESM) show that the exchange current density (j_0) of WC/WO_{3-x}-900 was 0.253 mA·cm^{-2}, which was markedly higher than that of bare WC, indicating the highest reaction efficiency. The ECSA was calculated by the C_{dl} obtained by the CV test (Fig. S12 in the ESM) [36]. The electrode WC/WO_{3-x}-900 displayed the highest C_{dl} of 181.8 mF·cm^{-2} (Fig. 6(c)) and the largest ECSA of 4545.0 cm^2 (Table S3 in the ESM). These results suggested that it had the largest electrocatalytic effective surface area, leading to the best performance.

The Nyquist plots (Fig. 6(d)), which were fitted into an equivalent circuit containing solution resistance (R_s), were used to investigate the electrochemical activity of the electrocatalysts in H_2SO_4 media and estimated the values of charge transfer resistance (R_{ct}) and constant phase element (CPE). The smallest radius, i.e., R_{ct} = 0.82 Ω, was recorded for WC/WO_{3-x}-900, which was much lower than that of WC (4.66 Ω), suggesting its superior electrical conductivity and reaction kinetics at

the electrocatalyst–electrolyte interface (Table S2 in the ESM). The FE of the HER of WC/WO_{3-x}-900 membrane electrode was evaluated, and the experimental measurement was consistent with the theoretically calculated amount of hydrogen, showing that the FE of the electrode was close to 100% (Fig. S13 in the ESM). The TOF was also measured to investigate the intrinsic activity of the electrodes. According to Fig. S14 in the ESM, the TOF value of WC/WO_{3-x}-900 was 2.37 s^{-1}, which was more than 5 times that of WC (0.42 s^{-1}) when the overpotential was 200 mV.

During the operation process of HER catalyst, durability and stability are important parameters, which define the electrode's performance. The linear sweep voltammetry (LSV) curves for WC/WO_{3-x}-900 before and after 10,000 CV cycles (Fig. 7(a)) were almost overlapped, suggesting robust durability. In addition, the chronopotentiometric curve test at 30, 50, 100, 200, and 400 mA·cm^{-2} was employed to evaluate the electrode stability (Fig. 7(b)). The overpotential remained almost constant under various current densities tested. Moreover, the overpotential of 30 mA·cm^{-2} remained almost constant after 180 h of operation, suggesting good long-term stability. Furthermore, after the stability test, no change was detected in the morphology, phase composition, and the chemical state of WC/WO_{3-x}-900, reflecting its excellent stability (Figs. S15 and S16 in the ESM). Considering the scouring and impact effect of water flow on the electrode in the actual process of water electrolysis, a water permeability test was performed on WC/WO_{3-x}-900 (Fig. S17 in the ESM). The water permeation flux was 12.08×10^3 L·m^{-2}·h^{-1}·bar^{-1}, which remained stable under 3.0 bar for 4 h. In addition, the LSV curves almost coincided before and after the test, which reflected the stable and practical performance of the membrane electrode.

The LSV plots of the prepared electrodes in comparison with Pt in alkaline media are presented in Fig. 8(a). Compared to the 234-mV overpotential of the bare WC electrode, WC/WO_{3-x}-900 manifested superior electrocatalytic activity with a low overpotential of 123 mV. The overpotential in alkaline solution was higher than that in acidic solution, which should be due to the protons provided by water dissociation under alkaline condition [59]. Moreover, the hydrophilicity of the electrode in acidic solution was better than that in alkaline solution, which should be conducive due to the full contact between the electrolyte and the electrode (Fig. S18 in the ESM) [41]. WC/WO_{3-x}-900 electrode also had the smallest Tafel slope of 72.4 mV·dec^{-1}, suggesting that the Volmer–Heyrovsky mechanism governed the catalytic process (Fig. 8(b) and Table S4 in the ESM). Additionally, the highest exchange current density (j_0) of 0.363 mA·cm^{-2} was recorded for WC/WO_{3-x}-900, which justified its excellent catalytic performance among the produced catalysts (Fig. S19 and Table S4 in the ESM). From the CV curves (Fig. S20 in the ESM), the C_{dl} of WC/WO_{3-x}-900 was calculated as 168.3 mF·cm^{-2}, approximately 8 times as high as that of WC (21.9 mF·cm^{-2}) (Fig. S21 and Table S4 in the ESM), and the calculated ECSA was 4207.5 cm^2 (Table S3 in the ESM). These results confirmed that this electrode exposed the highest number of reactive sites in alkaline media.

According to the Nyquist plots (Fig. S22 in the ESM), the charge transfer resistance (R_{ct}) of WC/WO_{3-x}-900 was 1.01 Ω, which was the smallest among the prepared electrodes. Moreover, the FE of WC/WO_{3-x}-900 was close to 100%, reflecting its high catalytic performance

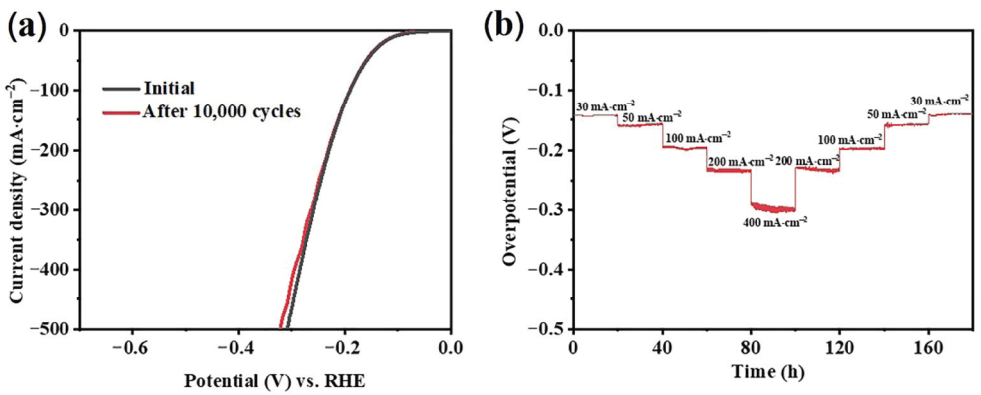

Fig. 7 HER performance of WC/WO_{3-x}-900 ceramic electrode in 0.5 M H_2SO_4. (a) Comparison of polarization curves before and after 10,000 CV cycles and (b) chronopotentiometry curve at 30, 50, 100, 200, and 400 mA·cm^{-2} for 180 h.

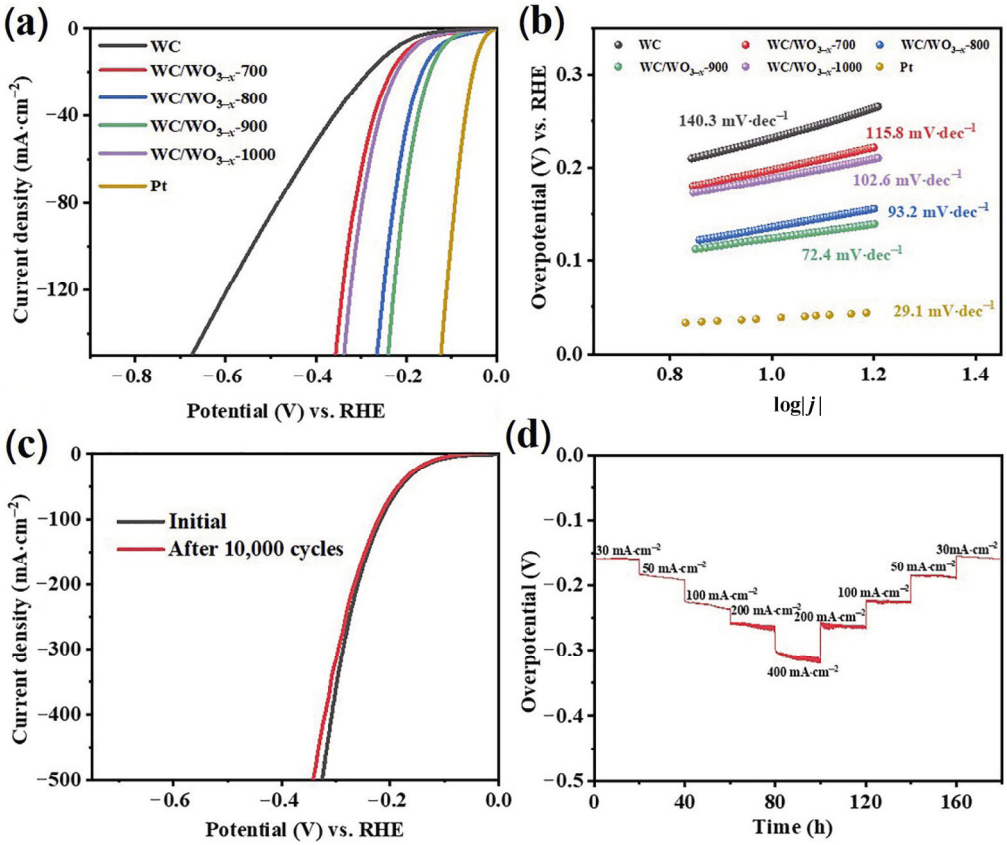

Fig. 8 HER performance of WC and WC/WO_{3-x}-*T* thermal-treated at 700, 800, 900, and 1000 ℃ and the comparison with commercial Pt wire electrode in 1.0 M KOH media. (a) Polarization curves, (b) Tafel slope plots, (c) comparison of polarization curves before and after 10,000 CV cycles, and (d) chronopotentiometry curve at 30, 50, 100, 200, and 400 mA·cm^{-2} for 180 h for WC/WO_{3-x}-900 ceramic electrode.

(Fig. S23 in the ESM). Meanwhile, WC/WO_{3-x}-900 also showed the highest intrinsic activity with a TOF value of 2.19 s^{-1} at an overpotential of 200 mV (Fig. S24 in the ESM). There were no striking differences in the LSV curves of WC/WO_{3-x}-900 before and after 10,000 CV cycles in the 1.0 M KOH solution (Fig. 8(c)), suggesting that the electrode also had good long-term HER stability in alkaline media. In addition, in the chronopotential curve test (Fig. 8(d)) at current densities of 30, 50, 100, 200, and 400 mA·cm^{-2}, the overpotential of 30 mA·cm^{-2} remained almost constant after 180 h of operation, suggesting its superior long-term stability in alkaline media. As expected, the morphology and phase composition of WC/WO_{3-x}-900 electrode were almost unaffected by the long-term stability test (Figs. S15 and S16 in the ESM).

The HER performance of WC/WO_{3-x}-900 was compared with the previously reported TC-based catalysts in acidic and alkaline media (Tables S5 and S6 in the ESM, respectively). The HER performance of WC/WO_{3-x}-900 electrode exceeded those of many TC-based electrocatalysts. Most importantly, WC/WO_{3-x}-900 was a strong self-supported electrode prepared through a simple and scalable production method.

The above experimental results showed that the WO_{3-x} whiskers produced by the reaction of WC with CO_2 should play an important role. The *in situ* developed WC/WO_{3-x} heterostructure interface synergistically modulated the electronic structure and the charge transfer, favoring the acceleration of the HER electrochemical process and the maintenance of high stability [22,60,61]. The appropriate number and diameter of WO_{3-x} in WC/WO_{3-x}-900 lead to the best HER performance. Furthermore, the abundance of oxygen vacancies in the non-stoichiometric WO_{3-x} provided many effective electron transfer paths, which could accelerate the electron transfer, and could also play the role of active sites to improve the HER performance [2,31,56]. They could also modulate the electronic structure and reduce the band gap of WO_3, and often generate interband states for WO_3, thereby improving conductivity [40,62]. Moreover, the *in situ*

high-temperature reaction generated many defects, which could modulate the electronic structure and surface properties of the electrodes, thereby optimizing the H adsorption step in the HER [63]. The high superhydrophilicity (Fig. S18 in the ESM) and the asymmetric structure favored the charge transfer between the electrode and the electrolyte as well as the easy removal of the bubbles from the electrode surface.

4 Conclusions

A self-supporting porous WC ceramic electrode was produced with WO_{3-x} whiskers produced *in situ* on the surface and inside the finger-like hole structure. WC/WO_{3-x}-900 electrode displayed outstanding HER activity in both acidic and alkaline media (overpotentials of 107 and 123 mV and Tafel slopes of 59.3 and 72.4 $mV \cdot dec^{-1}$, respectively), and good long-term stability and durability. The superior HER performance was attributed to the WC/WO_{3-x} heterostructure interface, the abundance of oxygen vacancies, the superhydrophilicity, and the asymmetric structure of the finger-like holes. The self-supporting electrodes were also produced easily. Thus, they manifest good prospects for large-scale production and a wide application in water splitting in conjunction with their good properties.

Acknowledgements

This research was supported by the National Natural Science Foundation of China (U1732115), the China National Petroleum Corporation (KD200121), the Science and Technology Department of Henan Province (222102230054), and the Henan Province Education Department of Key Scientific Research Project in Colleges and Universities (21B430012).

Electronic Supplementary Material

Supplementary material is available in the online version of this article at https://doi.org/10.1007/s40145-022-0604-4.

References

[1] Wan ZX, He QT, Qu Y, *et al*. Designing coral-like Fe_2O_3-regulated Se-rich $CoSe_2$ heterostructure as a highly active and stable oxygen evolution electrocatalyst for overall water splitting. *J Electroanal Chem* 2022, **904**: 115928.

[2] Xie C, Chen W, Du SQ, *et al*. *In-situ* phase transition of WO_3 boosting electron and hydrogen transfer for enhancing hydrogen evolution on Pt. *Nano Energy* 2020, **71**: 104653.

[3] Chen MZ, Jia YM, Li HM, *et al*. Enhanced pyrocatalysis of the pyroelectric $BiFeO_3$/g-C_3N_4 heterostructure for dye decomposition driven by cold–hot temperature alternation. *J Adv Ceram* 2021, **10**: 338–346.

[4] Wang FH, Xu X, Xia YP, *et al*. A novel CO_2-tolerant $Ba_{0.5}Sr_{0.5}Co_{0.8}Fe_{0.1}Ta_{0.1}O_{3-\delta}$ cathode with high performance for proton-conducting solid oxide fuel cells. *Int J Hydrogen Energ* 2021, **46**: 33561–33571.

[5] Yang L, Zhu XB, Xiong SJ, *et al*. Synergistic $WO_3 \cdot 2H_2O$ nanoplates/WS_2 hybrid catalysts for high-efficiency hydrogen evolution. *ACS Appl Mater Interfaces* 2016, **8**: 13966–13972.

[6] Mo ZY, Yang WY, Gao S, *et al*. Efficient oxygen reduction reaction by a highly porous, nitrogen-doped carbon sphere electrocatalyst through space confinement effect in nanopores. *J Adv Ceram* 2021, **10**: 714–728.

[7] Li PZ, Yang W, Tian CJ, *et al*. Electrochemical performance of $La_2NiO_{4+\delta}$–$Ce_{0.55}La_{0.45}O_{2-\delta}$ as a promising bifunctional oxygen electrode for reversible solid oxide cells. *J Adv Ceram* 2021, **10**: 328–337.

[8] Yu ZJ, Mao KW, Feng Y. Single-source-precursor synthesis of porous W-containing SiC-based nanocomposites as hydrogen evolution reaction electrocatalysts. *J Adv Ceram* 2021, **10**: 1338–1349.

[9] Yu HB, Qi LL, Hu Y, *et al*. Nanowire-structured FeP–CoP arrays as highly active and stable bifunctional electrocatalyst synergistically promoting high-current overall water splitting. *J Colloid Interface Sci* 2021, **600**: 811–819.

[10] Han NN, Yang KR, Lu ZY, *et al*. Nitrogen-doped tungsten carbide nanoarray as an efficient bifunctional electrocatalyst for water splitting in acid. *Nat Commun* 2018, **9**: 924.

[11] Zeng MQ, Chen YX, Li JX, *et al*. 2D WC single crystal embedded in graphene for enhancing hydrogen evolution reaction. *Nano Energy* 2017, **33**: 356–362.

[12] Bennett LH, Cuthill JR, McAlister AJ, *et al*. Electronic structure and catalytic behavior of tungsten carbide. *Science* 1974, **184**: 563–565.

[13] Levy RB, Boudart M. Platinum-like behavior of tungsten carbide in surface catalysis. *Science* 1973, **181**: 547–549.

[14] Houston JE, Laramore GE, Park RL. Surface electronic properties of tungsten, tungsten carbide, and platinum. *Science* 1974, **185**: 258–260.

[15] Chen ZY, Duan LF, Sheng T, *et al*. Dodecahedral W@WC composite as efficient catalyst for hydrogen evolution and nitrobenzene reduction reactions. *ACS Appl Mater Interfaces* 2017, **9**: 20594–20602.

[16] Lin JF, Pitkänen O, Mäklin J, *et al*. Synthesis of tungsten carbide and tungsten disulfide on vertically aligned multi-walled carbon nanotube forests and their application

as non-Pt electrocatalysts for the hydrogen evolution reaction. *J Mater Chem A* 2015, **3**: 14609–14616.

[17] Sun HM, Yan ZH, Liu FM, *et al*. Self-supported transition-metal-based electrocatalysts for hydrogen and oxygen evolution. *Adv Mater* 2020, **32**: 1806326.

[18] Xie LS, Li XL, Wang B, *et al*. Molecular engineering of a 3D self-supported electrode for oxygen electrocatalysis in neutral media. *Angew Chem Int Ed* 2019, **58**: 18883–18887.

[19] Lv K, Zheng DW, Shi YY, *et al*. Highly efficient and robust MoS_2 nanoflake-modified-TiN-ceramic-membrane electrode for electrocatalytic hydrogen evolution reaction. *ACS Appl Energy Mater* 2021, **4**: 6730–6739.

[20] Shi YY, Zheng DW, Zhang X, *et al*. Self-supported ceramic electrode of 1T–2H MoS_2 grown on the TiC membrane for hydrogen production. *Chem Mater* 2021, **33**: 6217–6226.

[21] An L, Huang BL, Zhang Y, *et al*. Interfacial defect engineering for improved portable zinc–air batteries with a broad working temperature. *Angew Chem Int Ed* 2019, **58**: 9459–9463.

[22] Wang FH, Wu YT, Dong BB, *et al*. Robust porous WC-based self-supported ceramic electrodes for high current density hydrogen evolution reaction. *Adv Sci* 2022, **9**: 2106029.

[23] Guo JY, Wang BZ, Yang DD, *et al*. Rugae-like Ni_2P–CoP nanoarrays as a bi-functional catalyst for hydrogen generation: $NaBH_4$ hydrolysis and water reduction. *Appl Catal B Environ* 2020, **265**: 118584.

[24] Tao S, Xu YD, Gu JQ, *et al*. Preparation of high-efficiency ceramic planar membrane and its application for water desalination. *J Adv Ceram* 2018, **7**: 117–123.

[25] Wang FH, Dong BB, Ke NW, *et al*. Superhydrophobic β-sialon–mullite ceramic membranes with high performance in water treatment. *Ceram Int* 2021, **47**: 8375–8381.

[26] Wu R, Zhang JF, Shi YM, *et al*. Metallic WO_2–carbon mesoporous nanowires as highly efficient electrocatalysts for hydrogen evolution reaction. *J Am Chem Soc* 2015, **137**: 6983–6986.

[27] Yang WY, Chen Y, Gao S, *et al*. Post-illumination activity of Bi_2WO_6 in the dark from the photocatalytic "memory" effect. *J Adv Ceram* 2021, **10**: 355–367.

[28] Yang YT, Shao X, Zhou SQ, *et al*. Interfacial electronic coupling of NC@WO_3–W_2C decorated Ru clusters as a reversible catalyst toward electrocatalytic hydrogen oxidation and evolution reactions. *ChemSusChem* 2021, **14**: 2992–3000.

[29] Liu Y, Shrestha S, Mustain WE. Synthesis of nanosize tungsten oxide and its evaluation as an electrocatalyst support for oxygen reduction in acid media. *ACS Catal* 2012, **2**: 456–463.

[30] Thalji MR, Ali GAM, Algarni H, *et al*. Al^{3+} ion intercalation pseudocapacitance study of $W_{18}O_{49}$ nanostructure. *J Power Sources* 2019, **438**: 227028.

[31] Chen JD, Yu DN, Liao WS, *et al*. WO_{3-x} nanoplates grown on carbon nanofibers for an efficient electrocatalytic hydrogen evolution reaction. *ACS Appl Mater Interfaces* 2016, **8**: 18132–18139.

[32] Remškar M, Kovac J, Viršek M, *et al*. W_5O_{14} nanowires. *Adv Funct Mater* 2007, **17**: 1974–1978.

[33] Peng QM, He QT, Hu Y, *et al*. Interface engineering of porous Fe_2P–$WO_{2.92}$ catalyst with oxygen vacancies for highly active and stable large-current oxygen evolution and overall water splitting. *J Energy Chem* 2022, **65**: 574–582.

[34] Li YX, Zhai XL, Liu Y, *et al*. WO_3-based materials as electrocatalysts for hydrogen evolution reaction. *Front Mater* 2020, **7**: 105.

[35] Feng CY, Tang L, Deng YC, *et al*. Synthesis of branched WO_3@$W_{18}O_{49}$ homojunction with enhanced interfacial charge separation and full-spectrum photocatalytic performance. *Chem Eng J* 2020, **389**: 124474.

[36] Hu GJ, Li J, Liu P, *et al*. Enhanced electrocatalytic activity of WO_3@NPRGO composite in a hydrogen evolution reaction. *Appl Surf Sci* 2019, **463**: 275–282.

[37] Liu D, Ren XW, Li YS, *et al*. Nanowires-assembled WO_3 nanomesh for fast detection of ppb-level NO_2 at low temperature. *J Adv Ceram* 2020, **9**: 17–26.

[38] Dong BB, Yang MY, Wang FH, *et al*. Porous Al_2O_3 plates prepared by combing foaming and gel-tape casting methods for efficient collection of oil from water. *Chem Eng J* 2019, **370**: 658–665.

[39] Diao JX, Qiu Y, Liu SQ, *et al*. Interfacial engineering of W_2N/WC heterostructures derived from solid-state synthesis: A highly efficient trifunctional electrocatalyst for ORR, OER, and HER. *Adv Mater* 2020, **32**: 1905679.

[40] Diao JX, Yuan WY, Qiu Y, *et al*. A hierarchical oxygen vacancy-rich WO_3 with "nanowire-array-on-nanosheet-array" structure for highly efficient oxygen evolution reaction. *J Mater Chem A* 2019, **7**: 6730–6739.

[41] Qian QZ, Zhang JH, Li JM, *et al*. Artificial heterointerfaces achieve delicate reaction kinetics towards hydrogen evolution and hydrazine oxidation catalysis. *Angew Chem Int Ed* 2021, **60**: 5984–5993.

[42] Hu Y, Yu B, Ramadoss M, *et al*. Scalable synthesis of heterogeneous W–W_2C nanoparticle-embedded CNT networks for boosted hydrogen evolution reaction in both acidic and alkaline media. *ACS Sustain Chem Eng* 2019, **7**: 10016–10024.

[43] Xu YT, Xiao XF, Ye ZM, *et al*. Cage-confinement pyrolysis route to ultrasmall tungsten carbide nanoparticles for efficient electrocatalytic hydrogen evolution. *J Am Chem Soc* 2017, **139**: 5285–5288.

[44] Li JH, You SJ, Liu MY, *et al*. ZIF-8-derived carbon-thin-layer protected WC/$W_{24}O_{68}$ micro-sized rods with enriched oxygen vacancies as efficient Pt co-catalysts for methanol oxidation and oxygen reduction. *Appl Catal B Environ* 2020, **265**: 118574.

[45] Kou ZK, Wang TT, Pu ZH, *et al*. Realizing the extraction

of carbon from WC for *in situ* formation of W/WC heterostructures with efficient photoelectrochemical hydrogen evolution. *Nanoscale Horiz* 2019, **4**: 196–201.

[46] Xiao P, Ge XM, Wang HB, *et al*. Novel molybdenum carbide–tungsten carbide composite nanowires and their electrochemical activation for efficient and stable hydrogen evolution. *Adv Funct Mater* 2015, **25**: 1520–1526.

[47] Meng J, Lin QY, Chen T, *et al*. Oxygen vacancy regulation on tungsten oxides with specific exposed facets for enhanced visible-light-driven photocatalytic oxidation. *Nanoscale* 2018, **10**: 2908–2915.

[48] Dong BB, Wang FH, Yu JL, *et al*. Production of calcium hexaluminate porous planar membranes with high morphological stability and low thermal conductivity. *J Eur Ceram Soc* 2019, **39**: 4202–4207.

[49] Hirata Y, Daio S, Kai A, *et al*. Performance of yttria-stabilized zirconia fuel cell using H_2–CO_2 gas system and CO–O_2 gas system. *Ceram Int* 2016, **42**: 18373–18379.

[50] Han BQ, Xu JL, Li N. Formation of Al_2O_3–WC powders from Al–WO_3–C mixtures. *Miner Process Extr Metall* 2006, **115**: 189–194.

[51] Behnami AK, Sakaki M, Bafghi MS, *et al*. Facile microwave-assisted fabrication of WC–Al_2O_3 composite powder from WO_3–Al–C mixture. *Trans Nonferrous Met Soc China* 2017, **27**: 2630–2637.

[52] Shen ZG, Zhao ZY, Qian JW, *et al*. Synthesis of WO_{3-x} nanomaterials with controlled morphology and composition for highly efficient photocatalysis. *J Mater Res* 2016, **31**: 1065–1076.

[53] Mohammadzadeh Valendar H, Rezaie H, Samim H, *et al*. Reduction and carburization behavior of NiO–O_3 mixtures by carbon monoxide. *Thermochimica Acta* 2014, **590**: 210–218.

[54] Liu WB, Song XY, Zhang JX, *et al*. A novel route to prepare ultrafine-grained WC–Co cemented carbides. *J Alloys Compd* 2008, **458**: 366–371.

[55] Wang Y, Liu HY, Wang K, *et al*. 3D interconnected hierarchically porous N-doped carbon with NH_3 activation for efficient oxygen reduction reaction. *Appl Catal B Environ* 2017, **210**: 57–66.

[56] Li W, Wang DD, Zhang YQ, *et al*. Defect engineering for fuel-cell electrocatalysts. *Adv Mater* 2020, **32**: 1907879.

[57] Wu ZX, Wang J, Liu R, *et al*. Facile preparation of carbon sphere supported molybdenum compounds (P, C and S) as hydrogen evolution electrocatalysts in acid and alkaline electrolytes. *Nano Energy* 2017, **32**: 511–519.

[58] Chen ZG, Gong WB, Cong S, *et al*. Eutectoid-structured WC/W_2C heterostructures: A new platform for long-term alkaline hydrogen evolution reaction at low overpotentials. *Nano Energy* 2020, **68**: 104335.

[59] Yao MQ, Wang BJ, Sun BL, *et al*. Rational design of self-supported Cu@WC core–shell mesoporous nanowires for pH-universal hydrogen evolution reaction. *Appl Catal B Environ* 2021, **280**: 119451.

[60] Hu Y, Yu HB, Qi LL, *et al*. Interface engineering of needle-like P-doped MoS_2/CoP arrays as highly active and durable bifunctional electrocatalyst for overall water splitting. *ChemSusChem* 2021, **14**: 1565–1573.

[61] Wang BZ, Huang HX, Huang ML, *et al*. Electron-transfer enhanced MoO_2–Ni heterostructures as a highly efficient pH-universal catalyst for hydrogen evolution. *Sci China Chem* 2020, **63**: 841–849.

[62] Asnavandi M, Yin YC, Li YB, *et al*. Promoting oxygen evolution reactions through introduction of oxygen vacancies to benchmark NiFe–OOH catalysts. *ACS Energy Lett* 2018, **3**: 1515–1520.

[63] Kim M, Anjum MAR, Choi M, *et al*. Covalent 0D–2D heterostructuring of Co_9S_8–MoS_2 for enhanced hydrogen evolution in all pH electrolytes. *Adv Funct Mater* 2020, **30**: 2002536.